Cement and Concrete Composites 146 (2024) 105380

Contents lists available at ScienceDirect

Cement and Concrete Composites

journal homepage: www.elsevier.com/locate/cemconcomp

Reactivity of kaolinitic clays calcined in the 650 °C–1050 °C temperature range: Towards a robust assessment of overcalcination

Franco Zunino [a,b,*], Karen Scrivener [a]

[a] Laboratory of Construction Materials, EPFL STI IMX LMC, École Polytechnique Fédérale de Lausanne, 1015, Lausanne, Switzerland
[b] Physical Chemistry of Building Materials, Institute for Building Materials (IfB), ETH Zürich, CH-8093, Zürich, Switzerland

ARTICLE INFO

Keywords:
Calorimetry
Kinetics
Pore size distribution
Metakaolin
Pozzolan

ABSTRACT

Using calcined clays as supplementary cementitious materials is one of the main solutions available for a substantial and widespread reduction of the clinker factor in cement. Thus, understanding the phenomena governing their production process and reactivity is crucial for a successful technological deployment. In this study, the mineralogical and physical changes experienced by kaolinitic clays calcined within 650 and 1050 °C were explored, with emphasis on the identification of overcalcination. It was observed that the decrease in reactivity above the optimum calcination temperature is associated with the formation of Al–Si spinel and a decrease in specific surface area, which is linked to a modification of the pore size distribution within the particles. Differential scanning calorimetry (DSC) was identified as the most robust, and repeatable technique to identify an overcalcined kaolinitic clay. In combination with thermogravimetric analysis (TGA), it can provide a complete calcination process overview, relevant for quality control purposes.

1. Introduction

Concrete is the substance used in the largest quantity by humanity, second only to water. The portland cement (PC) needed for its production accounts for roughly 8 % of manmade CO_2 emissions [1]. Among the alternatives to reduce the carbon footprint of the cement industry, the most promising one is to reduce the proportion of clinker by replacing part of it with supplementary cementitious materials (SCMs) [2]. Typically used SCMs include limestone, granulated blast furnace slag and fly ash.

On the contrary, clays and limestone are available in virtually unlimited quantities [2]. Limestone calcined clay cements (LC^3) are ternary blended cements that incorporate limestone and calcined kaolinitic clay together, replacing 50 % or more of the conventional PC. With 50 % replacement, a strength development similar to conventional PC is reached after 7 days of hydration [3–6]. The LC^3 technology enables to reduce the CO_2 emissions between 30-to-40 % per ton of cement produced compared to PC [6].

Clay minerals are made of particles comprised of stacks of hundreds of crystal layers. Each of these layers is on its own composed of alternating silica tetrahedral and alumina octahedral sheets [7,8]. The three main clay groups are kaolinite, illite and montmorillonite (smectite). Kaolinite is known as a 1:1 ratio clay, with a stacking sequence of one silicate (tetrahedral coordination) and one aluminate (octahedral coordination) sheet [9], while in illite and montmorillonite the stacks are made of two silicate sheets sandwiching an aluminate sheet (also known as 2:1 clays) [10]. Of the major clay types, kaolinite exhibits a higher pozzolanic reactivity after calcination [11]. Natural clays with different grades (i.e., kaolinite content) can be found [12], intermixed with other minerals such as quartz, limestone, iron bearing phases (responsible of color) and other rock forming minerals.

When heated, kaolinite ($Al_2O_3 \bullet 2SiO_2 \bullet 2H_2O$) is decomposed (dehydroxylated) in the temperature range between 400 and 650 °C [13]. The dehydroxylation of kaolinite leads to an amorphous material known as metakaolinite ($Al_2O_3 \bullet 2SiO_2$) [8,10,14], Equation (1). There is a well-known relationship between the stacking (dis)order of adjacent layers and the degree of dehydroxylation that can be achieved at a certain calcination temperature for a given clay [15–17]. In practice, raw clay is calcined in the range 700 and 800 °C to maximize the reactivity of the resulting material, which is related to the quantity and disorder of metakaolinite in the calcined clay. Several experimental techniques such as X-ray diffraction (XRD), thermogravimetric analysis (TGA), infrared spectroscopy (FTIR) or loss on ignition can be used as reliable tools to assess and verify the complete dehydroxylation of clay

* Corresponding author. Physical Chemistry of Building Materials, Institute for Building Materials (IfB), ETH Zürich, CH-8093, Zürich, Switzerland
E-mail address: franco.zunino@ifb.baug.ethz.ch (F. Zunino).

https://doi.org/10.1016/j.cemconcomp.2023.105380
Received 2 August 2023; Received in revised form 9 November 2023; Accepted 27 November 2023
Available online 2 December 2023
0958-9465/© 2023 The Authors. Published by Elsevier Ltd. This is an open access article under the CC BY license (http://creativecommons.org/licenses/by/4.0/).

Table 1
Chemical composition of both raw clays determined by XRF.

	NC	Ka
SiO_2	48.13	44.39
Al_2O_3	35.08	38.85
Fe_2O_3	9.44	0.57
CaO	0.81	0.03
Na_2O	0.20	0.29
K_2O	0.08	0.30
MnO	0.01	0.01
TiO_2	2.27	1.05
MgO	0.52	0.01
P_2O_5	0.34	0.05
SO_3	0.02	0.10
SSA (m^2/g)	52.25	12.39

[18].

At temperatures around 925–1050 °C, Al–Si cubic spinel ($Al_2O_3 \bullet 3SiO_2$) is formed, Equation (2) [19–21]. The structure of this phase has been studied in detail [21]. It has been established that Al–Si spinel formation is an independent process to mullite formation [20], with a structure characterized by the presence of alumina in octahedral and tetrahedral coordination [22]. At higher temperatures (>1050 °C) mullite is formed, Equation (3) [23]. Above 1200 °C, amorphous silica can crystallize into cristobalite. These simplified equations do not describe the complexity of the actual process (non-stoichiometric composition of the originating phases, gradual transformation, influence of kaolinite properties and assoc. minerals). Nevertheless, they provide a useful overview of the different reactions taking place.

$$\text{Dehydroxilation}: Al_2O_3 \bullet 2SiO_2 \bullet 2H_2O \xrightarrow{400-650^\circ C} Al_2O_3 \bullet 2SiO_2 + 2H_2O_{(g)} \quad (1)$$

$$\text{Al}-\text{Si Spinel}: 2(Al_2O_3 \bullet 2SiO_2) \xrightarrow{925-1050^\circ C} 2Al_2O_3 \bullet 3SiO_2 + SiO_{2(amorph)} \quad (2)$$

$$\text{Mullite}: 3(2Al_2O_3 \bullet 3SiO_2) \xrightarrow{>1050^\circ C} 2(3Al_2O_3 \bullet 2SiO_2) + 5SiO_{2(amorph)} \quad (3)$$

In terms of pozzolanic reactivity, it has been observed that kaolinitic clay calcined at temperatures above 900 °C exhibit considerably lower reactivity compared to the same materials calcined at lower tempera-

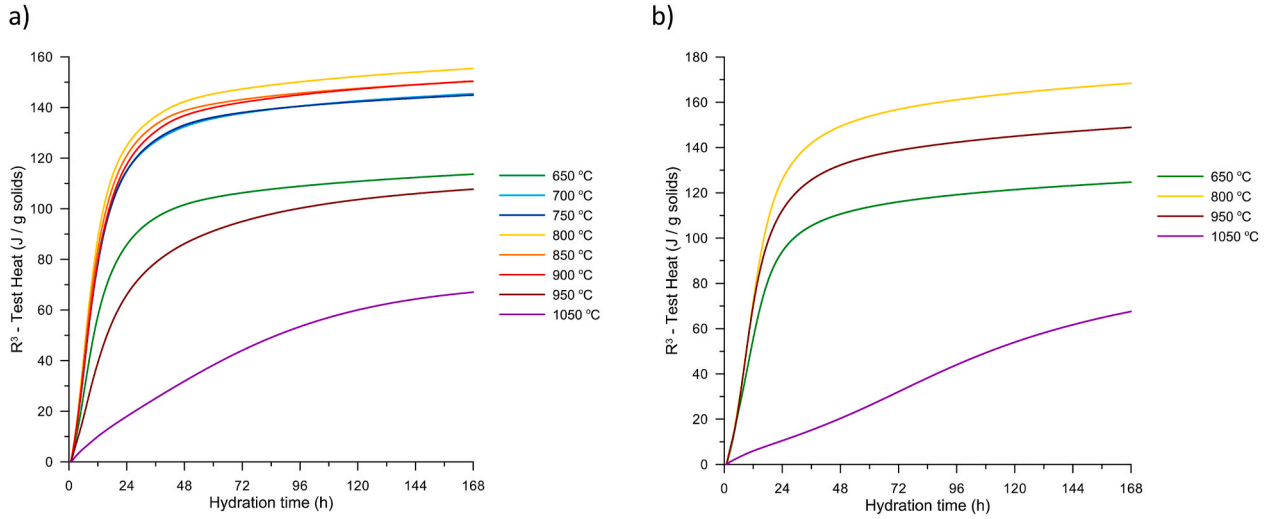

Fig. 1. Heat released (R^3 reactivity test) by NC (a) and Ka (b) clays calcined at different temperatures. (Conversion factor {J/g SCM}/{J/g solids} = 4.5).

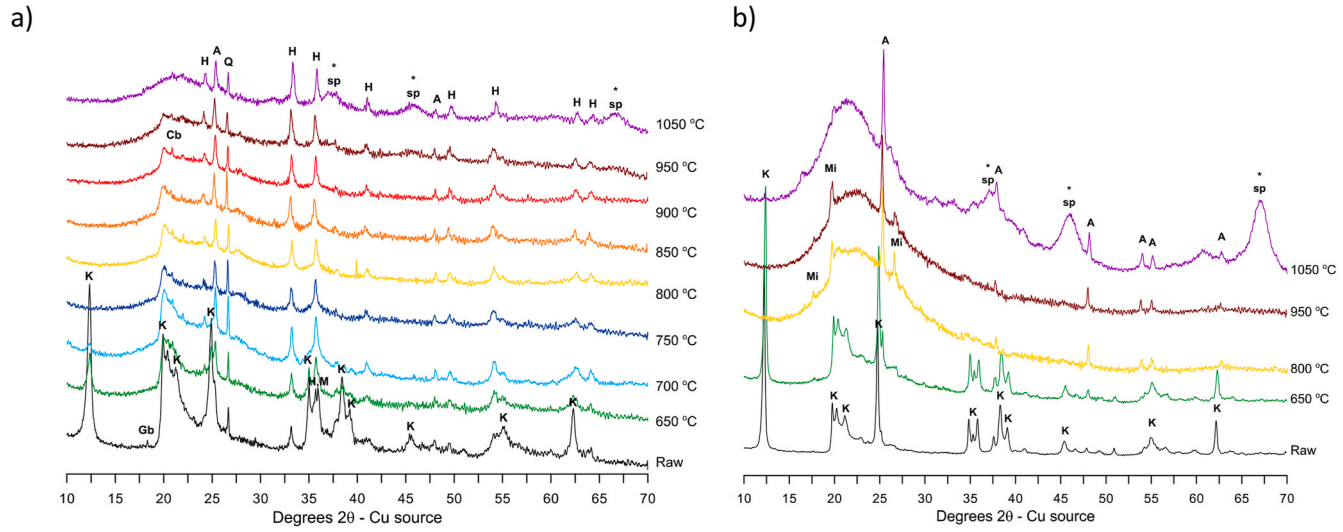

Fig. 2. Diffraction pattern of NC (a) and Ka (b) clays calcined at different temperatures
K: kaolinite; Gb: gibbsite; Cb: cristobalite; M: magnetite; Q: quartz; H: hematite; A: anatase; Mi: mica; sp: Al–Si spinel.

Table 2
Summary of reactivity of NC and Ka clays calcined at different temperatures, and normalized reactivities referred to the 800 °C samples (ratios at 24 h and 7 days of reaction are presented). (Conversion factor {J/g SCM}/{J/g solids} = 4.5).

	Natural clay (NC)				Kaolinite (Ka)			
	R^3@24h (J/g sol.)	R^3@168h (J/g sol.)	R^3@24h/R^3@24h (800)	R^3@168h/R^3@168h (800)	R^3@24h (J/g sol.)	R^3@168h (J/g sol.)	R^3@24h/R^3@24h (800)	R^3@168h/R^3@168h (800)
650 °C	85.8	113.7	0.69	0.73	94.1	124.7	0.75	0.74
700 °C	114.9	145.4	0.92	0.94	–	–	–	–
750 °C	114.9	144.9	0.92	0.93	–	–	–	–
800 °C	124.9	155.4	**1.00**	**1.00**	125.9	168.4	**1.00**	**1.00**
850 °C	121.0	150.3	0.97	0.97	–	–	–	–
900 °C	117.5	150.4	0.94	0.97	–	–	–	–
950 °C	65.9	107.7	0.53	0.69	112.3	148.9	0.89	0.88
1050 °C	17.9	67.0	0.14	0.43	10.5	67.6	0.08	0.40

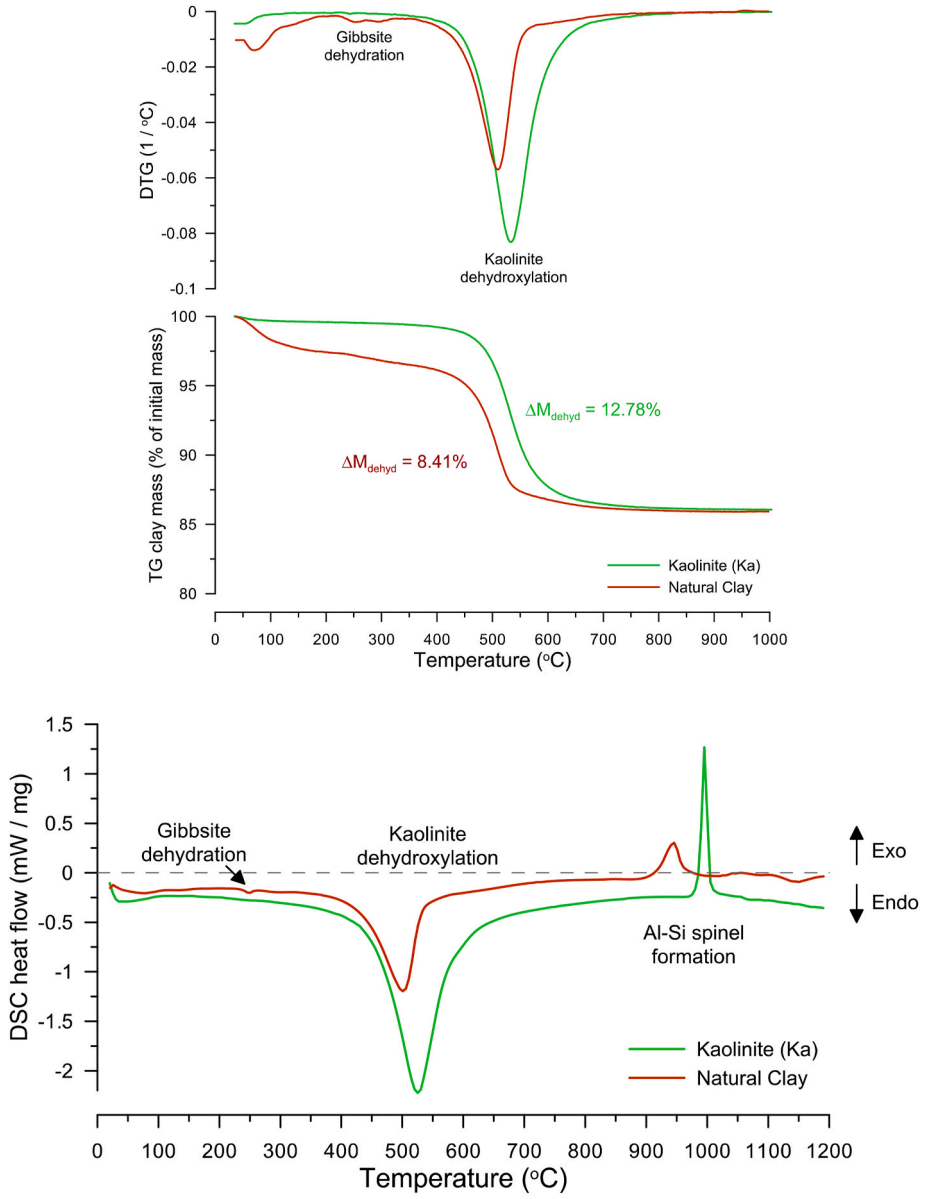

Fig. 3. TG/DTG curves (top) and DSC curves (bottom) of natural clay (NC) and Ka samples. The main features observed with both techniques are highlighted.

tures [8,11,13], a condition that is commonly referred as over-calcination. The decrease in reactivity has been attributed to the sintering of clay particles which increases particle size and reduces surface area [8] or to the crystallization of mullite [24]. However, the formation of Al–Si spinel which should occur before mullite, has not received much attention. This reaction occurs at constant mass, and therefore gravimetric approaches cannot be used to characterize it. Moreover, the association of reactivity loss solely to mullite formation may give the impression that the temperature range for optimal calcination and the temperature at which overcalcination starts are further apart than in

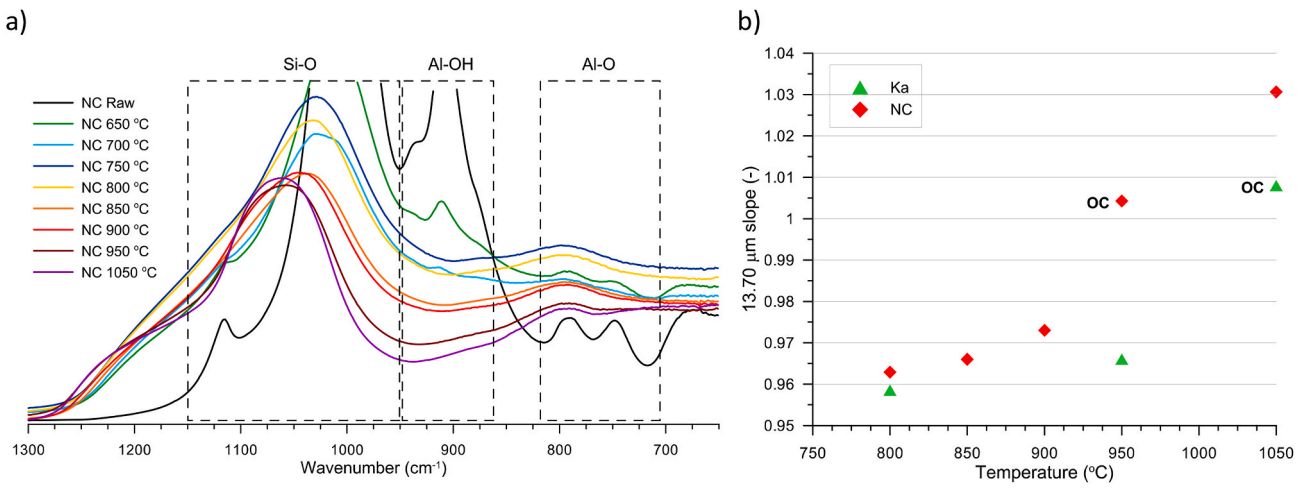

Fig. 4. FTIR spectra of different NC samples represented as ATR-FTIR absorbance (shifted for clarity) versus wavelength, showing the main spectral absorption bands seen in this wavelength range (a) and 13.70 slope parameter indicating the variation of the Al–O absorption band (b).

reality.

The R^3-test provides a reliable and reproducible test to assess the reactivity of calcined clay [25]. However, it takes at least 24 h to obtain a result, which makes it unsuitable for real time production control. FTIR has been proposed as a fast tool to characterize high-temperature transformations of kaolinite [26]. However, it has the disadvantage of requiring a series of samples of the same material, calcined at different temperatures for comparison. To ensure adequate quality control during industrial production of calcined (kaolinitic) clays, overcalcination needs to be better understood, and a rapid, easy-to-interpret methodology to assess overcalcination is urgently needed. Differential scanning calorimetry (DSC) has been extensively used for decades to study the mineralogy of kaolinitic clay [27,28]. The work of Speil et al. [27] shows that the technique can be successfully used to characterize the Al–Si spinel peak irrespective of the associated minerals present and even for different minerals of the kaolin group. It also highlights that the position and broadness of the peak depends on the particle size of kaolinite.

This paper explores the transformations of kaolinitic clay during calcination in the 650–1050 °C temperature range, with a specific focus to the less explored higher temperature at which spinel formation takes place. The reactivity and the evolution of physical properties are assessed and related to the mineralogical transformations of high purity kaolinite. In addition to more routine characterization methods (XRD, TGA, FTIR), solid-state magnetic nuclear resonance (NMR) is used to provide further insights on the arrangement and structure of the phases formed. The potential of DSC to assess overcalcination is explored.

2. Materials and methods

2.1. Raw materials

Two different kaolinitic clay were used in this study. The first one is a natural clay (NC, from Chile) with 60 % kaolinite content as measured by thermogravimetric analysis (TGA). The second clay is a low iron, high kaolinite content clay (Ka, 90 % kaolinite content) that is used as raw feed to produce high purity metakaolin. The NC was ground in a ball mill with 20 L capacity for 2 h. Ka was received ground from the manufacturer. The chemical composition by X-ray fluorescence (XRF) of both clays is shown in Table 1. The higher purity material (Ka, no iron-bearing associated minerals) enabled more detailed investigations on the relationship of calcination temperature and reactivity, such as ^{27}Al solid state nuclear magnetic resonance.

2.2. Calcination, physical and mineralogical characterization

The clays were calcined by placing 50 g of the raw clay in 200 mL alumina crucibles. The crucibles were then placed in a laboratory furnace and heated to the desired calcination temperature at about 10 °C/min. The maximum temperature was held for 30 min and the crucibles were left to cool down inside the furnace until 300 °C, at which point they were removed and air cooled to room temperature. In the case of the NC, samples were calcined to maximum temperatures of 650, 700, 750, 800, 850, 900, 950 and 1050 °C. For the Ka samples, the maximum temperatures were 650, 800, 950 and 1050 °C as they were observed to be representative of the different reactivity/mineralogical conditions in NC samples.

X-ray diffraction (XRD) was used to assess the mineralogical composition of the clays. The diffraction patterns were acquired using back loaded powder holders to reduce the effects of preferred orientation. The samples were measured in Bragg–Brentano mode using an X'Pert PANalytical diffractometer with CuKα source operated at 45 kV and 40 mA. Each clay sample was scanned from 7 to 70° 2θ with a step size of 0.0167 2θ, equivalent to a time per step of 60 s. Rietveld refinement of the patterns of raw clay was conducted using Highscore Plus using a rutile external standard to account for presence of amorphous phases. The XRD analysis presented does not intent to be exhaustive (particularly in terms of sample preparation) to the level required for an exhaustive quantitative analysis of clay minerals [18], but rather provide a reference on the ability of the technique to reliably identify overcalcined clays through a quick assessment of presence/absence of certain reflections of interest.

The kaolinite content was determined by **thermogravimetric analysis (TGA)** in a Mettler Toledo analyzer (TGA/SDTA 851). The temperature was increased between 30 and 1000 °C with a heating ramp of 10 °C/min. The atmosphere used was N_2 at a flow rate of 30 mL/min. The tangent method was used for the determination of the weight loss associated with kaolinite dehydroxylation.

In addition to TGA, **differential scanning calorimetry (DSC)** was used to assess the transformations of the clays that do not involve mass variations. A Netzsch DSC 404 C high-temperature analyzer was used for the measurements. A sample of clay of 30–35 mg was placed in a platinum crucible with a perforated lid. Another empty crucible of the same type was used as reference. The purge atmosphere used was argon (Ar) with a flow rate of 50 mL/min. The temperature was increased from 30 °C to 1200 °C and the heat flow recorded over this range.

Particle size distributions (PSD) were determined by laser diffraction using a Malvern S device. First, the clay was dispersed by adding approximately 0.1 g of material to 50 mL of a 0.01 % aqueous

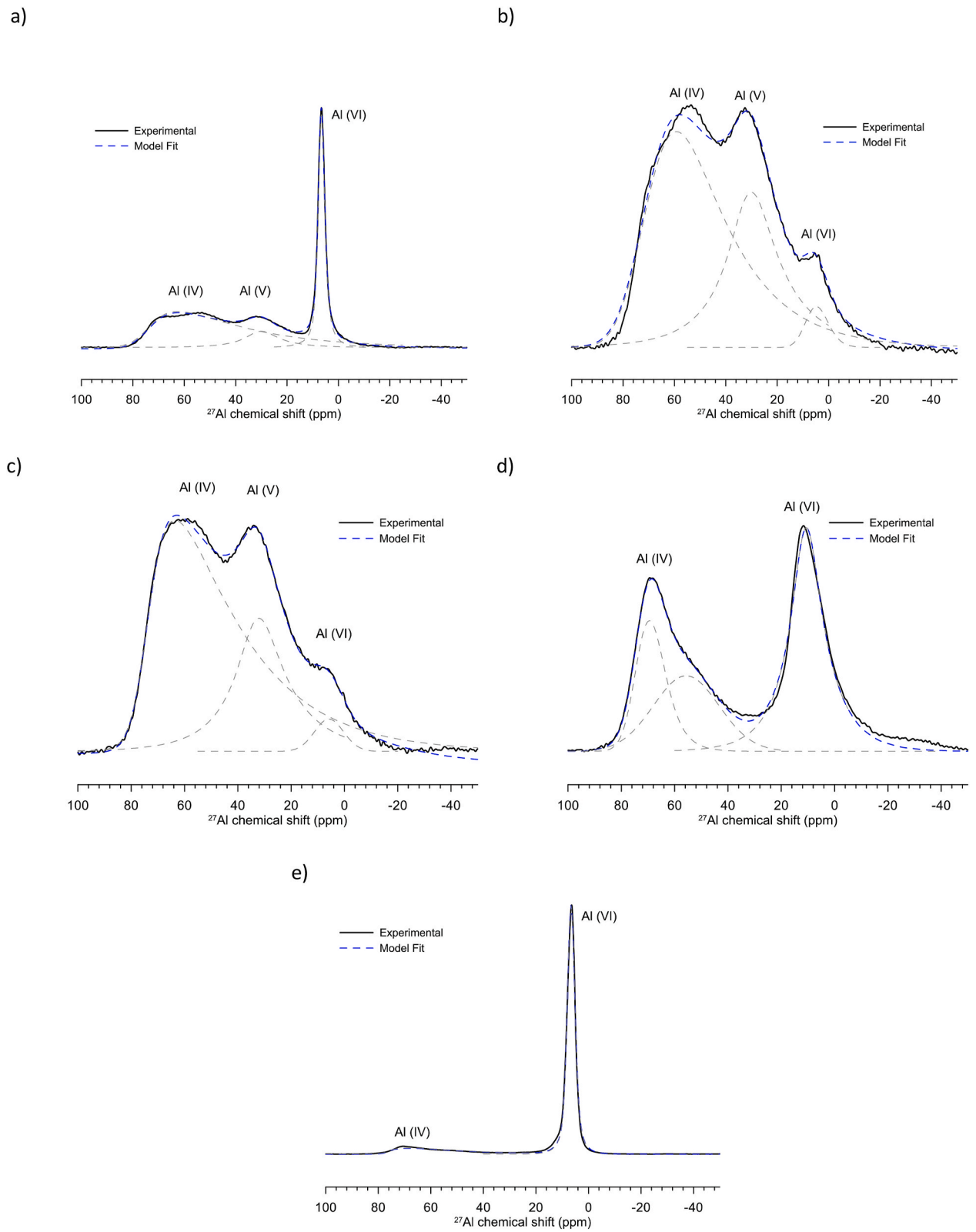

Fig. 5. ^{27}Al MAS NMR spectra of Ka samples calcined at 650 °C (a), 800 °C (b), 950 °C (c),1050 °C (d) and Raw (e). The Czsimple fitting of each spectrum is shown in dashed lines.

solution of sodium hexametaphosphate, which deagglomerates and disperses kaolinite particles [29]. The suspension was then transferred to an ultrasonic probe for 15 min. Drops of the resulting suspension were transferred to the measuring unit filled with distilled water, until the desired level of obscuration (10–12 %) was reached. The optical model was set as prescribed in Ref. [30], considering an imaginary component of the refractive index of 0.01 for clay NC (red material) and 0.001 for Ka (white material).

The specific gravity of the raw and calcined clay was measured by **helium (He) pycnometry**. The measurement was conducted

Table 3
Quadrupolar coupling constants (C_Q, KHz) and chemical shifts (δ_{ppm}) computed from the MAS NMR spectra (Czsimple model).

	Raw		650 °C		800 °C		950 °C		1050 °C	
	δ_{ppm}	C_Q	δ_{ppm}	C_Q	δ_{ppm}	C_Q	δ_{ppm}	C_Q	δ_{ppm}	C_Q
Al(IV)	77	14.0	75	15.7	73	13.5	75	15.0	73/59	5.9/4.7
Al(V)	–	–	31	3.3	31	4.7	33	4.8	–	–
Al(VI)	7	1.7	7	2.1	8	5.0	7	3.7	11	3.1

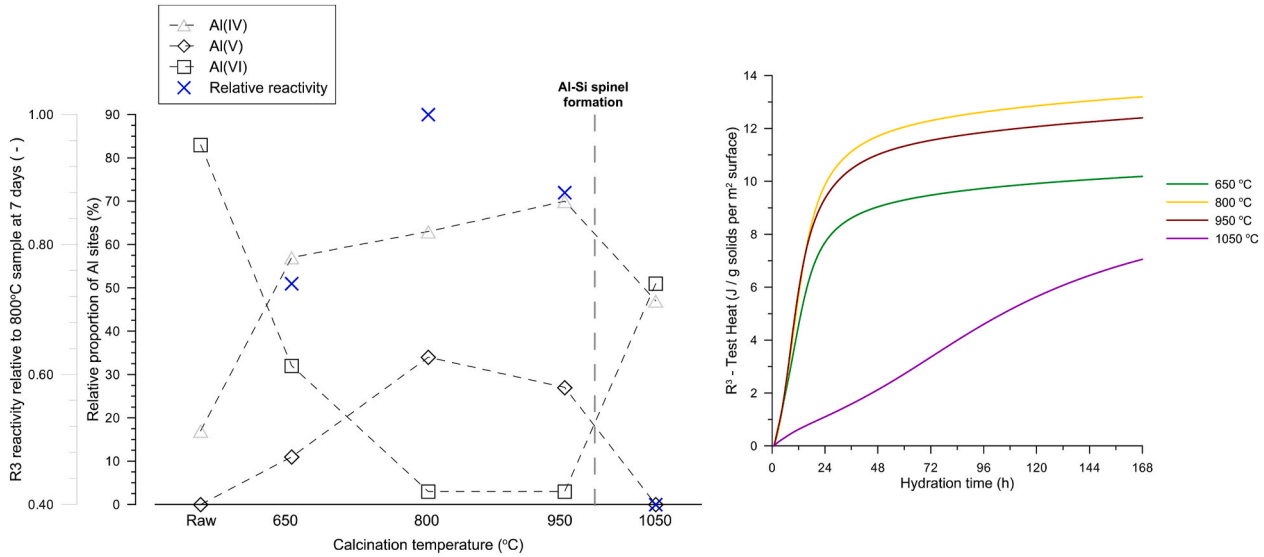

Fig. 6. Evolution of Al sites determined by fitting and deconvolution of the central transitions of ^{27}Al MAS NMR spectra of Ka samples (a) where the relative reactivity (referred to the 800 °C maximum) is shown for comparison. Reactivity of Ka samples normalized by specific surface area (b).

immediately after cooling following calcination, as it was observed that the humidity of the clay influenced significantly the results. The measurements were conducted in a 20 cm^3 calibrated cell. About 2 g of material were placed in the cell, and 10 purging cycles with He were done up to a pressure of 19.5 psig (psi gauge, referred to ambient pressure). Following the purging cycles, 20 measuring cycles were conducted up to the same maximum pressure, and the equilibrium condition was fixed to a variation at or below 0.005 psig/min between the measuring and reference cells.

2.3. Reactivity, surface and particle properties of calcined clay

The reactivity of the calcined clays was assessed using **isothermal calorimetry** based on the R^3 reactivity method [25]. In this procedure, calcined clay is mixed with portlandite, calcium carbonate and a solution of potassium sulphate and hydroxide. The sample is transferred to a glass ampoule and placed in a TAM Air isothermal calorimetry calibrated at 40 °C for up to 7 days.

^{27}Al solid state unidimensional (1D) high-field magic angle spinning nuclear magnetic resonance (MAS NMR) was carried out on the Ka samples (no iron) to characterize the different aluminum sites present after calcination at each temperature. The spectra were recorded on a 900 MHz Bruker spectrometer (21.1 T) equipped with an Avance NEO console and a 3.2 mm three-channel low temperature MAS probe. Sample spinning was set to 24 kHz, and a one-pulse $\tau = 0.7$ μs sequence was used, corresponding to less than $\tau_{90}/12$ for uniform excitation of the full signal, including spinning side bands and satellite transitions. A total of 1024 transients were cumulated for every spectrum with a recovery delay greater than $1.3T_1$. The chemical shifts were referenced to a 1.1 m $Al(NO_3)_3$ aqueous solution.

Solid-state ^{27}Al 3QMAS NMR spectra were recorded to establish the number of different Al sites present (quadrupolar nuclei, spin $I = 5/2$) and their approximate chemical shift to enable accurate deconvolution and quantification of the 1D spectra on a 700 MHz Bruker spectrometer (16.4 T) equipped with an Avance III console and a 2.5 mm two-channel CPMAS probe. The analysis of the 3QMAS spectra is the only mean to establish with certainty the number and distribution of the sites for deconvolution of the 1D spectra. Samples were packed into 2.5 mm zirconia rotors and spun up at 20 kHz spinning speed. Powdered Al $(acac)_3$ was used as secondary reference for chemical shifts (0.15 ppm relative to 1.1 m $Al(NO_3)_3$ in H_2O) [31]. The ^{27}Al 3QMAS NMR spectra were acquired using a 3-pulse *experiment with a split-T1 and full echo acquisition* [32]. The excitation, conversion, and detection pulses lasted 4.75, 12.7, and 38 μs, respectively. Up to 90 T_1 slices of 1200–4800 scans were acquired with a T_1 increment of 25 μs and the spectra were processed using the Topspin (Bruker) software.

The dmfit software [33] was used to fit the 3QMAS spectra and to deconvolute and fit the central transitions of the 1D spectra obtained based on the 3QMAS fits. The minimum number of peaks (described by Czjzek distributions) was used to fit the spectra leaving position, intensity and width free to fit. In all cases, the selected distribution to deconvolute that the spectrum is recorded at infinite spinning speed (Czsimple model).

Fourier transform infrared spectroscopy (FTIR) measurements were conducted to complement the information obtained from XRD, using a 6700 Nicolet spectrometer by Thermo Fischer Sci. An attenuated total reflectance (ATR) accessory was used for the measurements, equipped with a diamond crystal and a potassium bromide (KBr) beam splitter. The spectra were recorded in the long-to- mid wave infrared (MWIR and LWIR) range, between wavenumbers 4000 and 625 cm^{-1} (2.5–16 μm in wavelength). A total of 32 background and sample scans were taken for each individual sample, with a resolution of 2.0 cm^{-1}. The 13.7 μm slope parameter, proposed in Ref. [26] as a means to assess overcalcination, was computed in each case after background

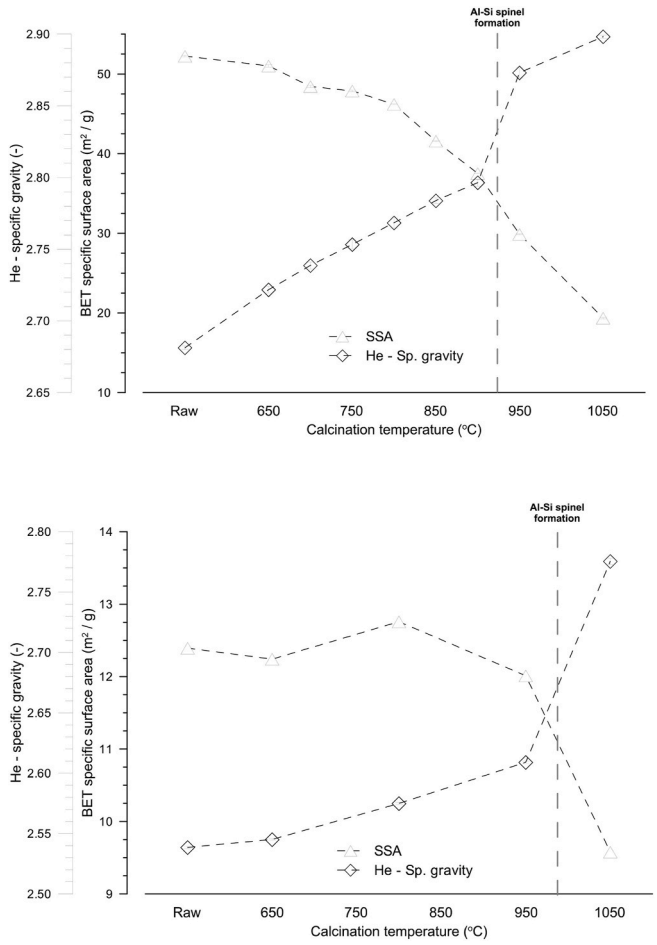

Fig. 7. Evolution of specific surface area (nitrogen adsorption) and specific gravity (helium pycnometry) versus temperature of calcination of NC (top) and Ka (bottom) samples.

Table 4
Particle size distribution percentiles (10 %, 50 % and 90 %) for the different raw and calcined clay measured by laser diffraction. Overcalcined materials are shown in bold font.

	Natural clay (NC)			Kaolinite (Ka)		
	D_V10 [μm]	D_V50 [μm]	D_V90 [μm]	D_V10 [μm]	D_V50 [μm]	D_V90 [μm]
Raw	0.15	5.56	37.61	0.94	6.23	17.97
650 °C	0.17	4.71	38.51	1.97	6.95	18.94
700 °C	0.16	4.59	37.30	–	–	–
750 °C	0.17	4.61	43.00	–	–	–
800 °C	0.18	5.19	44.50	2.91	7.65	19.03
850 °C	0.17	5.25	44.80	–	–	–
900 °C	0.17	5.41	44.85	–	–	–
950 °C	**0.19**	**7.04**	**59.48**	3.11	8.69	24.23
1050 °C	**0.20**	**7.40**	**59.30**	**2.62**	**8.75**	**28.75**

subtraction and normalization of the curves was conducted. It is computed as the ratio between the reflectance intensity at 13.3 μm (751.8 cm^{-1}) and 13.75 μm (727.7 cm^{-1}).

The specific surface area and particle porosity were studied by **nitrogen adsorption**. A sample of 1 g of clay was placed in the apparatus and degassed at 200 °C for 2 h under a N_2 flux. After degassing, the tubes containing the samples were transferred to their measuring position in a Micromeritics Tristar apparatus. Isotherms were collected for relative pressure (P/P_0) values between 0 and 1. The linear portion of the isotherm (0–0.3 P/P_0) enables the computation of the specific surface area by application of the BET method. A pore size distribution was obtained by applying the Barett-Joyner-Halenda (BJH) method to the full isotherms, enabling a decouple of the surface contribution of the different pore sizes present in the clay particles.

3. Results and discussion

3.1. Reactivity measurements and characterization of clays via XRD, FTIR, TGA and DSC

The total heat release measured in the isothermal calorimetry reactivity tests [25] is shown in Fig. 1 for NC (Fig. 1a) and Ka (Fig. 1b) clays (precision for single operator determined at 10 J/g of SCM). Fig. 2 shows the diffraction patterns of the corresponding materials. The associated minerals present in NC and their abundance quantified by Rietveld refinement are quartz (25 %), hematite and magnetite (9.7 % combined), gibbsite (3 %) and anatase (<1 %). In the case of Ka, the associated minerals are mica (3 %) and anatase (5 %).

In both cases, the maximum reactivity is observed for the material calcined at 800 °C. At 650 °C, dehydroxylation is not complete in both clays, as evidenced by the presence of the basal (11° 2θ) and other peaks of kaolinite. At 700 and 750 °C, the peak is no longer observed for the NC clay indicating full amorphization. However, the observed reactivity continues to increase up to an optimum for the material calcined at 800 °C.

Above 800 °C, the reactivity of NC decreases slightly at 900 °C. In general terms, the reactivity of NC between 700 °C and 900° remains within a 10 % of the optimum condition (800 °C), Table 2. At 950 °C, a reduction in reactivity is seen for both materials. The magnitude of the reduction is quite different between the two clays: 47 % in the case of NC, and only 11 % in the case of Ka (Table 2). In both cases, the presence of Al–Si spinel is not evident at this temperature from the XRD pattern shown in Fig. 2. At 1050 °C, the reduction in reactivity increases considerably. For NC, the reduction in reactivity is 86 % compared to the one observed at 800 °C, while for Ka it is 92 %. In both cases, the presence of spinel is observed in the diffraction patterns, Fig. 2. It should be noted that additional sample preparation measures such as orientation and removal of the non-clay fraction may provide higher sensitivity to detect small amounts of spinel than those observed in this study [18].

Fig. 3 shows the TG/DTG curves for both clays (top) and the DSC curves for the same materials (bottom). As extensively reported, TGA can be used to assess kaolinite dehydroxylation (and compute the (uncalcined) kaolinite content) by measuring the weight loss between 400 and 650 °C [34], associated to the volatilization of water from the material. At higher temperatures, particularly in the range where reactivity is observed to decrease, there is no mass variation of the material. It should be noted that the referred temperature range for dehydroxylation is valid for TGA experiments but not necessarily for static (furnace) calcination, as seen in Fig. 2 where kaolinite is clearly seen after calcination at 650 °C. Other factors such as fineness, atmosphere and vapor pressure play a role in defining the dehydroxylation temperature in different conditions [13]. Other factors such as the stacking disorder can influence the temperature at which dehydroxylation takes place for a fixed set of experimental conditions [15,17].

The DSC curves shows the dehydroxylation of kaolinite in the same temperature range seen by TGA as an endothermic reaction. At higher temperatures, the formation of Al–Si spinel is seen as an exothermic, sharp peak starting around 900 °C for NC and 975 °C for Ka clay. By comparing Figs. 1 and 3, it can be seen that the position of the Al–Si peak corresponds well with the temperature at which the decrease in reactivity is seen. Thus, the reactivity loss of calcined clays due to overcalcination can be linked with a mineralogical transformation that can be reliable measured and described by DSC. Moreover, this technique enables an easy assessment of the whole calcination process of the material, accounting for its particularities (different temperature of the onset of spinel formation), by observation of the different decomposition

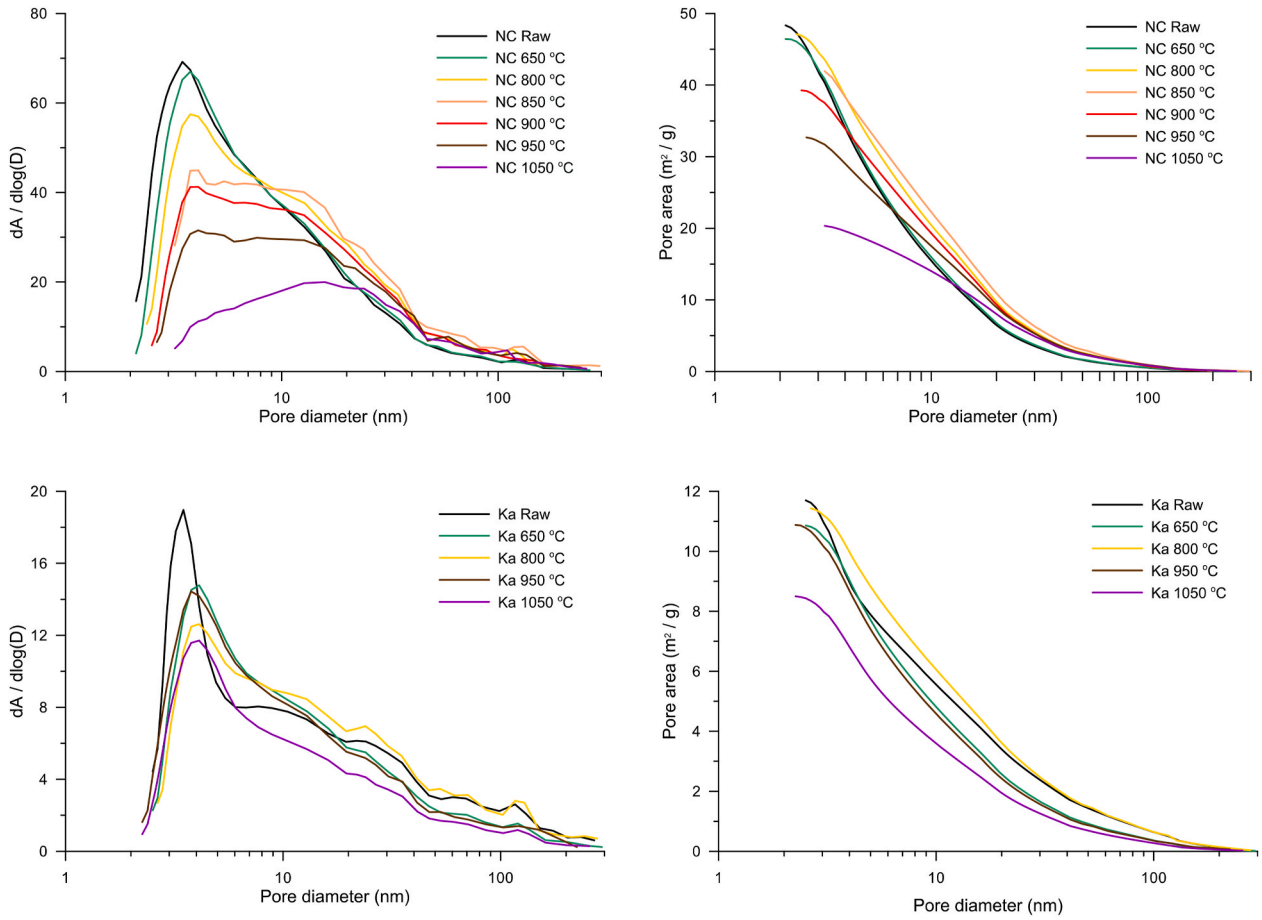

Fig. 8. Differential (left) and cumulative (right) particle pore surface computed using the BJH method based on nitrogen adsorption isotherms for NC (top) and Ka (bottom) calcined clay.

peaks.

- An **undercalcined clay** would have the endothermic peak of dehydroxylation between 400 and 650 °C and the spinel formation peak at 900–1000 °C as in Fig. 3 bottom, where the curves correspond to the raw materials.
- A **properly calcined clay** (fully dehydroxylated kaolinite) will not show the endothermic dehydroxylation peak at 400–650 °C, but the spinel formation peak at higher temperatures is present. Amorphization (and reactivity) continues to increase above 650 °C.
- An **overcalcined clay** would neither exhibit the endothermic dehydroxylation peak nor the spinel peak at higher temperatures, indicating that both transformations already took place (i.e., the temperature for spinel formation was exceeded).

As discussed in Ref. [35], kaolinite is concentrated in the finer particles of the size distribution in natural ground clays, and (harder) associated minerals such as quartz and feldspars remain coarser (25 % quartz + 9.7 % iron oxides in NC). In these materials, the presence of these hard phases leads to finer grinding of the clay minerals. Consequently, the different temperature for the occurrence of the spinel peak between NC and Ka is attributed to the finer kaolinite particles present in NC as compared to Ka, Fig. 1. An additional factor contributing to this difference might be a difference in the initial degree of disorder of the kaolinites, in addition to its known influence in the dehydroxylation temperature. The Hinckley index [36] and the Aparicio-Galan-Ferrell index (AGFI) [37] were determined from the XRD patterns of the raw clays [38] to assess the degree of disorder of kaolinite in both materials, yielding values of 0.78/0.28 for NC and 0.96/0.65 for Ka (AGFI/HI). Based on these indicators, kaolinite in NC is a highly defective kaolinite while Ka is a medium defective kaolinite [37].

Fig. 4a shows the FTIR spectra of the NC samples in the 1300 to 650 cm^1 wavelength range, corresponding to the aluminosilicate and Al–OH bands. The Al–OH band is barely visible in the 700 °C sample and disappears above this temperature, indicating complete dehydroxylation in agreement with XRD results, Fig. 2. The intensity of the Si–O band also reduces with calcination. The main change is observed above 850 °C, where the absorbance band narrows and shifts to shorter wavelengths. The Al–O bands become shallower, almost flat, after complete dehydroxylation. At shorter wavelengths (higher wavenumbers, between 4000 and 1300 cm^{-1}) bands associated with outer hydroxyl and molecular water [18,26,39]. These are indicative of the dehydroxylation process, but do not provide significant information regarding Al–Si spinel formation.

Crystallization of metakaolin have been associated with an increase in absorbance at longer wavelengths in the Al–O band [26]. This change is quantified by the 13.7 μm slope parameter, and the computed values for NC and Ka samples are shown in Fig. 4b. The values for NC are higher as compared to others previously reported [26] where pure kaolinite minerals where used. The values computed for Ka are closer to the ones reported in the literature. As NC contains gibbsite (Fig. 3) the values for the 13.7 μm slope parameter could be affected, but not at the temperatures where spinel formation is expected.

No clear linear correlation (R^2 computed 0.75 considering datapoints for both clays) between the two clays is observed as reported in Ref. [26], where R^2 values above 0.90 are reported, indicating that the 13.7 μm parameter is influenced by the properties of the clay (particle size of clay minerals and/or presence of associated minerals).

Table 5
Summary of advantages and disadvantages of test methods to discriminate properly calcined from overcalcined kaolinitic clay.

Method	Advantages	Disadvantages
DSC	Reliable detection of the Al–Si formation, fast (2–3h) and robust. Can be associated to TGA in some devices.	Some DSC devices cannot reach the temperature required for Al–Si spinel formation (high-temperature unit required).
Calorimetry (R^3)	Robust and reliable method, well established in the industry and standardized by ASTM.	It takes at least 24 h to obtain a result that enables identification of an overcalcined clay.
XRD	Fast (minutes if no special sample preparation is needed), widely available technique, no quantitative analysis required.	Identifying the Al–Si spinel peaks is challenging, especially clay containing numerous assoc. minerals.
FTIR	Fast measurement (seconds to few minutes), easy sample preparation if an ATR device is available. Potential for future development.	Variability and lack of standard patterns for interpretation and comparison. Overcalcination features are subtle. Possible interference with Al–O bearing associated minerals.
^{27}Al MAS NMR	Direct assessment of aluminum species in the clay, which can be associated to the formation of Al–Si spinel.	Difficult to use, expensive equipment that requires an expert operator. In most cases, this technique is only accessible by research institutions.
PSD	Fast (minutes), already available technique in many industrial laboratories.	No clear variation between properly and over calcined materials makes discrimination difficult.
SSA (BET)	Well-known technique, relatively fast (2–3 h including sample preparation for SSA measurement).	No clear discrimination between properly and overcalcined clay. Requires access to liquid nitrogen.
Sp. Gravity	Fast method (30 min–1 h), equipment readily available in industrial laboratories.	Extremely sensitive to humidity content of the clay. More data is needed to establish generalized correlations between overcalcination and sp. gravity.

Consequently, it is not possible to establish a general criterion to determine if a material is overcalcined or not with the data gathered in this study. If FTIR is complemented with R^3-tests to determine the reactivity of each sample, a correlation with the slope parameter might be possible by establishing a master curve. Further investigation is needed to assess the sensitivity of this method in materials with lower kaolinite content and where other aluminum oxides are present as associated minerals (gibbsite, corundum), which would interfere in this spectral range. However, the feasibility of acquiring data within minutes could play in favor of this technique in an industrial setup.

3.2. 27Al site distributions of calcined clay studied by ^{27}Al MAS/3QMAS NMR

Fig. 5 shows the ^{27}Al MAS NMR spectra for the different Ka samples studied. At 650 °C, the kaolinite is only partially dehydroxylated (Fig. 2b). The appearance of Al(V) and Al(IV) sites is visible, in contrast with the dominance of Al(VI) coordination (octahedral sites) in raw kaolinite. At 800 °C and 950 °C (fully dehydroxylated material but before spinel formation) a sharp increase in Al(V) and Al(IV) sites is observed along with a reduction of Al(VI), indicating disruption of the initial crystalline lattice seen in kaolinite [24]. Al(V) sites are associated with disordered structures [40], and previous studies have attributed the occurrence of Al(V) sites in metakaolin to the reactivity observed in the material [41].

At 1050 °C (Fig. 7d), when Al–Si spinel is formed, the Al(V) sites reduce significantly and the Al(VI) ones increase. This shift has been previously associated with formation of mullite [42]. However, as shown in this study, mullite is not detected by XRD (Fig. 2b) and the exothermic transformation corresponds solely to spinel formation rather than a coupled spinel/mullite crystallization [20]. The structure for the Al–Si spinel phase proposed by Low and McPherson is in agreement with the dominance of Al(IV) (tetrahedral sites) and Al(VI) (octahedral sites) in this phase. An interesting observation in this spectrum is the presence of a second, broad peak centered around 59 ppm. The information provided by 3QMAS experiments indicate that it is unlikely that these sites correspond to the same kind of Al(V), but rather Al(IV) or Al(V) sites with a higher degree of disorder.

The central transitions of each spectrum were fitted using Czjzek lines based on the number and nature of species determined on the 3QMAS experiments (Fig. A3). The quadrupolar coupling constants (C_Q) and the chemical shifts for each Al site identified are summarized in Table 3. Fig. 6 shows the evolution of Al sites versus temperature, along with the relative reactivity (referred to 800 °C) of the materials. The raw kaolinite contains a majority (around 80 %) of Al(VI) sites (octahedral coordination) and about 20 % of Al(IV) sites. As the calcination temperature increases, Al(IV) and Al(V) sites increase and Al (VI) sites decrease. Between 650 °C and 800 °C, the amount of Al(V) sites increase, associated with a decrease in the amount of Al(VI) sites. The proportion of Al(V) sites in fully dehydroxylated kaolinite is 34 % at 800 °C and 27 % at 900 °C, in agreement with previous studies [42]. The reactivity varies between these 2 experimental points, even normalizing the reactivity values by SSA (Table A1), Fig. 6b, which seems to be in accordance with the amount of Al(V) sites present. In the case of the 1050 °C material, despite the lower reactivity observed, the lack of Al(V) sites indicate a contribution of Al(IV) and/or Al(VI) to the reactivity of the material. The maximum reactivity seen for 800 °C seem to be associated with the simultaneous presence of Al(IV) and Al(V) sites.

Overall, the NMR characterization of the Ka samples seem to indicate that reactivity cannot be completely attributed to Al(V), but rather to a combined contribution of disordered Al sites occurring at different stages of the amorphization-crystallization process.

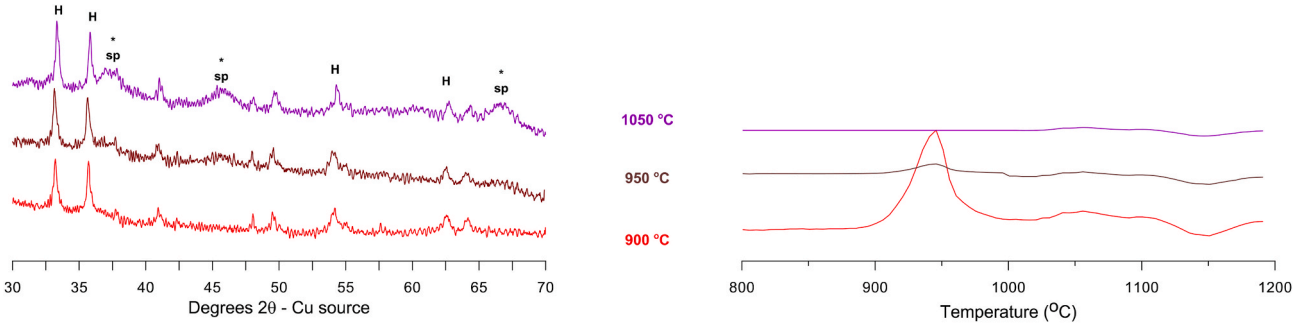

Fig. 9. XRD (left) and DSC (right) curves of NC clays calcined at 900 (properly calcined), 950 and 1050 °C (overcalcined).

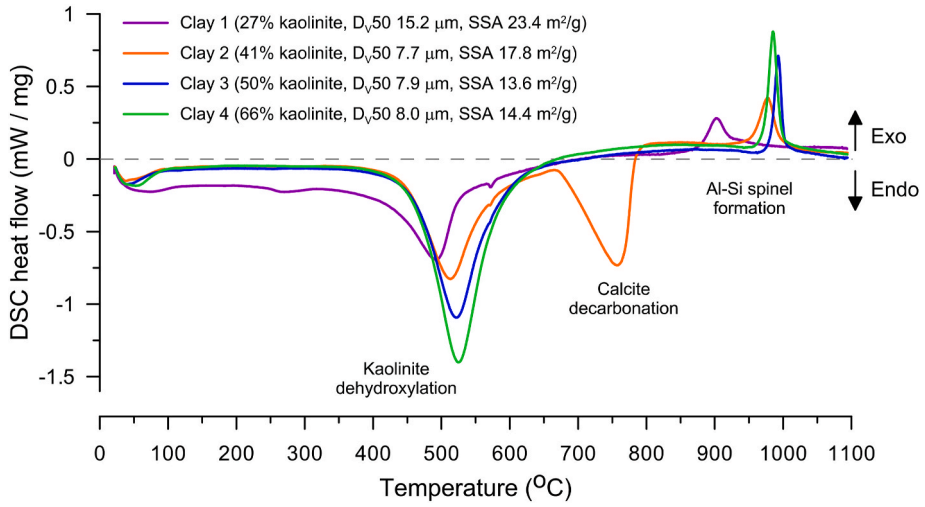

Fig. 10. DSC curves of natural kaolinitic clay with different kaolinite contents. Associated minerals include muscovite (1-3-4), calcite (2), anhydrite (1), quartz (all), albite (1–3), gibbsite (1-3-4) and hematite (all).

3.3. Evolution of porosity and surface area of calcined clays studied by nitrogen adsorption

As previously shown, differences in reactivity are observed between clays calcined at different temperatures even within the properly calcined temperature range (i.e., fully dehydroxylated kaolinite and before spinel formation). This is likely due to different degrees of amorphization (linked to reactivity) between these fully dehydroxylated materials. To further study these differences, the physicochemical changes that clay particles undergo upon calcination and the corresponding changes in reactivity and examined in this section.

The different calcined clay samples were analyzed by nitrogen adsorption. The monolayer adsorbed quantity (Q_0), the specific surface area determined using the BET method (S_{BET}) and the model constant (C_{BET}) are summarized in Table A1 of the appendix. Q_0 gives an indication of the amount of nitrogen adsorbed in a monolayer, while C_{BET} is related to the energy of adsorption, being proportional to the magnitude of the nitrogen/surface interactions. Fig. 7 shows a graphical representation of S_{BET} and specific gravity (He pycnometry) evolution versus temperature of calcination.

In the case of NC, the amount of nitrogen adsorbed decreases with calcination temperature, and S_{BET} follows a similar trend. A sharp decrease in surface area is seen after spinel formation (above 900 °C) In the case of Ka, the decrease in surface is also observed after spinel formation (above 950 °C). The decrease is more pronounced in Ka, most likely due to its higher kaolinite content. Nevertheless, surface area measurements provide a clear distinction of properly and over calcined material. The interaction (related to C_{BET}) between nitrogen and the surface decreases with calcination temperature, which is related to the sustained decrease in adsorbed amount of nitrogen (Q_0). Interestingly, after spinel formation, C_{BET} increases again in both materials despite the significantly lower Q_0, highlighting the change of mineralogy as previously presented (see Table A1).

In terms of specific gravity (Fig. 7), a continuous increase is observed with calcination temperature. After spinel formation, a sharp increase in specific gravity is observed for both materials. This suggests the possibility of using a volumetric method to assess overcalcination. However, the reliability of this approach should be established by systematic assessment over a wider range of samples, and the effect of preconditioning needs to be further studied.

Helium pycnometry measures the volume of a given mass of material by comparing the volume of a calibrated cell with the volume of helium that can occupy the accessible spaces of the sample. Thus, an increase in specific gravity is associated with a higher accessibility of helium to the pores and/or the formation of new porosity during Al–Si spinel formation. It was observed that this measure was extremely sensitive to the moisture condition of powders, which could vary significantly (changes greater than 25 %) in short periods of time (less than an hour) when the clay samples are exposed to ambient conditions.

Table 4 shows the particle size distribution percentiles determined by laser diffraction for each individual raw and calcined clay. Over-calcined materials, determined by DSC (Fig. 3) are shown in bold. In the NC material, there is a slight trend of increase in particle size with increase in calcination temperature. After formation of Al–Si spinel, a sharp increase in D_V50 and D_V90 is seen, which could be associated with interparticle sintering. In the case of Ka, this increase is not as clear as in the case of NC. This could suggest that the presence of impurities (particularly iron oxide) might influence the extent of interparticle sintering observed, phenomenon that has been observed with iron sulfides intermixed with kaolinite at similar calcination temperatures [43]. As previously stated, the finer particle size of NC might be a contributing factor to the lower temperature onset of spinel formation compared to Ka.

Fig. 8 shows the differential and cumulative internal pore areas (inner surface) for each calcined clay determined from the full adsorption isotherms (Fig. A2 in supplementary information) using the BJH method for NC (top) and Ka (bottom). In the cumulative pore area curves, the highest point of the curve approaches the SSA determined by BET for each material. In comparison to BET, the advantage of this approach is that it provides a relationship between surface area and the size of the defects/pores in the particles where it originates, similar to a porosity versus size curve obtained by mercury intrusion porosimetry (MIP).

As the calcination temperature increases, a continuous decreasing trend in porosity between 2 and 20 nm is seen for both materials, leading to the sustained decrease in SSA shown in Fig. 5. Interestingly, the decrease in small porosity is accompanied by coarsening of the threshold pore size compared to the raw clay (characterized as the inflection point of the cumulative curve, in analogy with MIP analysis). This indicates that different (larger) pores are being formed during Al–Si spinel formation. This increase could explain the increase in specific gravity with calcination temperature (Fig. 7), as the average pore becomes larger allowing easier accessibility for helium to the internal volume of the (meta)kaolinite particles. After spinel formation, an increase in the rate of porosity reduction below 20 nm is observed, leading to a considerable reduction in total specific surface area.

Along with particle size assessment (Table 4), these results show that the reduction of surface area in clay on calcination is associated with the

evolution of morphological features (small pores) inside the (meta) kaolinite particles, in agreement with observations made by electron microscopy [44]. While evidence of some degree of coarsening/interparticle sintering was observed in NC (increase of D_V50 upon overcalcination), this cannot fully explain the reduction in specific surface area measured.

3.4. Comparison of reliability and potential of methods to assess overcalcination

In this study, different methods were used to characterize kaolinitic calcined clay. Several of these methods, such as XRD, TGA, and FTIR can be used to assess dehydroxylation of the material. Others, such as the R^3-test and solid-state NMR provide additional insights on the reactivity or amorphization of the material after complete dehydroxylation, respectively. The formation of Al–Si spinel leading to the reduction in reactivity is, however, difficult to assess using these widely adopted techniques.

Table 5 presents a summary of advantages and disadvantages of the different methods explored in this study regarding the assessment overcalcination of kaolinitic clay, i.e., in their ability to accurately discriminate between a properly calcined clay and an overcalcined clay. Based on these considerations, DSC appears to be the most feasible method as it enables a direct, fast, robust and repeatable observation of Al–Si spinel formation. Furthermore, the approach required for overcalcination assessment is qualitative, and consequently no calibration or quantitative analysis of the data is required. Moreover, DSC (heat flow) signal can be collected in simultaneous TGA/DSC devices that are already widely available in the market for research and industrial applications and conventional alumina crucibles can be used. Other methods, such as FTIR and specific gravity measurements show potential for future development. However, the lack of standardization of FTIR makes interpretation of results challenging, and the influence of sample moisture in specific gravity measurements might compromise their suitability for quality control. On the contrary, the fast acquisition time of FTIR plays in favor and could open possibilities for use if further developments in this direction are pursued.

In the end, establishing a robust method to assess overcalcination of kaolinitic clays implies that discrimination of properly and overcalcined clays can be done reliably and unbiased by the operator. The potential of DSC over XRD (likely the most widely available technique in cement plants for mineralogical control) is highlighted in Fig. 9 for clay NC. While the spinel peaks are clearly visible at 1050 °C, they are difficult to identify in the 950 °C material (also overcalcined) referred to the material calcined at 900 °C (properly calcined) as comparison basis. This issue is likely accentuated for lower kaolinite content clays. In contrast, DSC provides a much clearer distinction between properly and overcalcined clay using the same comparative basis.

The robustness of DSC as a method to assess overcalcination of kaolinitic clay was further verified on a set of natural clay with different kaolinite contents ranging from 27 % up to 66 % and with different associated minerals, Fig. 10. In all cases the main associated mineral is quartz, with abundances estimated by Rietveld refinement of 21.1–13.5-16.2–6.8 % by mass for Clays 1-2-3-4, respectively (see Fig. A4 in the supplementary information for the full diffraction patterns of these clays). Clay 2 contains calcite (2.4 %), which decomposes over the same range of temperature and can interact with kaolinite [39]. Nevertheless, the spinel peak is still observable and thus can provide a reliable assessment on the calcination of the natural clay, independent of their kaolinite content and the presence of other minerals. An important insight is that the position of the onset of the spinel peak varies from around 890 °C to slightly above 1000 °C for the clays analyzed. This further highlights the need of a method to characterize this transformation for each material, as an overall temperature limit cannot be assumed.

As previously shown [27], the position of the spinel peak depends not only on the mineralogy (type of clay mineral and stacking fault density) but also on the physical characteristics (particle size) of the clay. The D_V50 and SSA of the clays are shown in the legend of the figure to illustrate this relationship. Iron content is also likely to affect the position of the exothermic peak [45]. Nevertheless, DSC appears to be a robust solution to determine the overcalcination temperature threshold accounting for all these factors. Clays 1, 3 and 4 contain muscovite (3.4, 22.8 and 7.6 % respectively) which can dehydroxylate in the temperature range of 800–900 °C [18]. This endothermic decomposition doesn't seem to inhibit the ability of DSC to observe the exothermic spinel crystallization. Nevertheless, in the case of mixed clays with higher amounts of 2:1 minerals (smectites and/or micas), additional measurements should be conducted to validate the observations presented in this article.

In practice, DSC measurements could be implemented for regular control of calcination (both dehydroxylation and overcalcination in one test), in a similar manner as XRD is used today. As in principle no quantitative analysis is needed, there is the possibility to explore higher heating rates to shorten experimental time and increase the output of the device. Developing reliable and robust sampling procedures is crucial as in large calcination devices (rotary kiln or flash calciner), temperature variations within the calcined material [13] may lead to partial overcalcination in some regions of the output feed. Homogenization and overall reactivity of the final material are the key parameters that should be considered to establish an industrial control protocol.

4. Conclusions

This study presents a comprehensive assessment of calcination temperature on the reactivity and mineral transformations of a natural kaolinitic clay and pure kaolinite. The mechanism leading to the decrease of reactivity beyond complete dehydroxylation (overcalcination) was identified, and a methodology to reliably assess overcalcination in calcined kaolinitic clay was proposed.

Based on the results presented, the following conclusions can be drawn.

1. The decrease in reactivity of overcalcined kaolinitic clay is associated with the formation of Al–Si spinel. The spinel formed exhibits a small crystallite size, making identification of the phase by XRD challenging. Spinel crystallization is associated with an exothermic peak that can be detected by DSC analysis.
2. DSC analysis of calcined kaolinitic clay can be used as a fast and reliable and industry suitable method to assess if a given calcined kaolinitic clay is overcalcined. The presence/absence of the spinel peak can be used as a qualitative indication without the requirement of reference materials for comparison.
3. The temperature at which Al–Si spinel crystallization (i.e., overcalcination) takes place depends on each clay (varying more than 100 °C among the clays studied) and therefore, a maximum calcination temperature to avoid overcalcination cannot be established without identifying the crystallization temperature in each case (for example, by DSC).
4. While less reactive than metakaolin, spinel exhibits some degree of pozzolanic activity. The variation in reactivity between fully dehydroxylated kaolinitic clay is partially linked to a decrease in surface area with calcination temperature. This decrease is associated with a reduction in small pores (<20 nm) in the clay mineral particles. On the contrary, interparticle sintering cannot explain the observed decrees in surface area.
5. Reactivity of kaolinitic clay cannot be fully explained by the presence of Al(V) sites. Spinel (overcalcined sample) exhibits only Al(IV) and Al(VI) sites, in agreement with previously proposed structures for this phase, and a non-negligible reactivity per unit surface area.

Declaration of competing interest

The authors declare that they have no known competing financial interests or personal relationships that could have appeared to influence the work reported in this paper.

Data availability

Data will be made available on request.

Acknowledgements

The authors would like to acknowledge financial support by the Swiss Agency of Development and Cooperation (SDC) grant 81026665. Dr. Zunino is supported by the Swiss National Science Foundation (SNSF) through an Ambizione fellowship (grant 208719). Andrea Teixeira and Eloïse Lurkin is acknowledged for her assistance in conducting the DSC experiments presented. The contribution of Dr. Laura Piveteau from EPFL-ISIC on conducting and analysing the NMR experiments presented here is greatly acknowledged, along with the insightful discussions on the paper. Dr. René Verel from the Laboratory of Inorganic Chemistry at ETH Zürich is also greatly acknowledged for conducting the 3QMAS measurements shown in this study.

Appendix A. Supplementary data

Supplementary data to this article can be found online at https://doi.org/10.1016/j.cemconcomp.2023.105380.

References

[1] T. Boden, B. Andres, G. Marland. Global CO2 Emissions from Fossil-Fuel Burning, Cement Manufacture, and Gas Flaring, Carbon Dioxide Information Analysis Center, Oak Ridge National Laboratory, Oak Ridge, 2017. https://cdiac.ess-dive.lbl.gov/trends/emis/tre_glob.html.

[2] K.L. Scrivener, V. John, E.M. Gartner, Eco-efficient Cements: Potential, Economically Viable Solutions for a low-CO2, Cement-Based Materials Industry, United Nations Environmental Programme (UNEP), 2016.

[3] F. Avet, K. Scrivener, Investigation of the calcined kaolinite content on the hydration of limestone calcined clay cement (LC3), Cement Concr. Res. 107 (2018) 124–135, https://doi.org/10.1016/j.cemconres.2018.02.016.

[4] F. Zunino, K. Scrivener, The reaction between metakaolin and limestone and its effect in porosity refinement and mechanical properties, Cem, Concr. Res. 140 (2021), https://doi.org/10.1016/j.cemconres.2020.106307.

[5] F. Zunino, F. Martirena, K. Scrivener, Limestone calcined clay cements (LC3), ACI Mater. J. 118 (2021) 49–60, https://doi.org/10.14359/51730422.

[6] K. Scrivener, F. Avet, H. Maraghechi, F. Zunino, J. Ston, W. Hanpongpun, A. Favier, Impacting factors and properties of limestone calcined clay cements (LC ^{3}), Green Mater. 7 (2019) 3–14, https://doi.org/10.1680/jgrma.18.00029.

[7] B. Sabir, S. Wild, J. Bai, Metakaolin and calcined clays as pozzolans for concrete: a review, Cem. Concr. Compos. 23 (2001) 441–454, https://doi.org/10.1016/S0958-9465(00)00092-5.

[8] A. Alujas, R. Fernández, R. Quintana, K.L. Scrivener, F. Martirena, Pozzolanic reactivity of low grade kaolinitic clays: influence of calcination temperature and impact of calcination products on OPC hydration, Appl. Clay Sci. 108 (2015) 94–101, https://doi.org/10.1016/j.clay.2015.01.028.

[9] J.W. Gruner, The crystal structure of kaolinite, Z. Für Krist. - Cryst. Mater. 83 (1932) 75–88.

[10] M. Antoni, Investigation of Cement Substitution by Combined Addition of Calcined Clays and Limestone, École Polytechnique Fédérale de Lausanne, 2011.

[11] R. Fernandez, F. Martirena, K.L. Scrivener, The origin of the pozzolanic activity of calcined clay minerals: a comparison between kaolinite, illite and montmorillonite, Cement Concr. Res. 41 (2011) 113–122, https://doi.org/10.1016/j.cemconres.2010.09.013.

[12] A. Ito, R. Wagai, Global distribution of clay-size minerals on land surface for biogeochemical and climatological studies, Sci. Data 4 (2017), 170103, https://doi.org/10.1038/sdata.2017.103.

[13] Theodore Hanein, Karl-Christian Thienel, Zunino Franco, T. Alastair, Matthias Maier Marsh, Bin Wang, Mariana Canut, C. Maria, G. Juenger, Mohsen Ben Haha, François Avet, Anuj Parashar, A. Layth, Al-Jaberi, Roger S. Almenares Reyes, Adrián Alujas Diaz, Karen L. Scrivener, Susan A. Bernal, L. John, Tongbo Sui Provis, Shashank Bishnoi, Fernando Martirena Hernández, Clay calcination technology: state-of-the-art review by the RILEM TC 282-CCL, Mater. Struct. 55 (2022) 3. https://doi.org/10.1617/s11527-021-01807-6.

[14] A. Souri, H. Kazemi-Kamyab, R. Snellings, R. Naghizadeh, F. Golestani-Fard, K. Scrivener, Pozzolanic activity of mechanochemically and thermally activated kaolins in cement, Cement Concr. Res. 77 (2015) 47–59, https://doi.org/10.1016/j.cemconres.2015.04.017.

[15] V.A. Drits, A. Derkowski, B.A. Sakharov, B.B. Zviagina, Experimental evidence of the formation of intermediate phases during transition of kaolinite into metakaolinite, Am. Mineral. 101 (2016) 2331–2346, https://doi.org/10.2138/am-2016-5776.

[16] A. Gualtieri, M. Bellotto, Modelling the structure of the metastable phases in the reaction sequence kaolinite-mullite by X-ray scattering experiments, Phys. Chem. Miner. 25 (1998) 442–452, https://doi.org/10.1007/s002690050134.

[17] G.W. Brindley, C.-C. Kao, J.L. Harrison, M. Lipsicas, R. Raythatha, Relation between structural disorder and other characteristics of kaolinites and dickites, Clay Clay Miner. 34 (1986) 239–249, https://doi.org/10.1346/CCMN.1986.0340303.

[18] R. Snellings, R. Almenares Reyes, T. Hanein, E.F. Irassar, F. Kanavaris, M. Maier, A. T. Marsh, L. Valentini, F. Zunino, A. Alujas Diaz, Paper of RILEM TC 282-CCL: mineralogical characterization methods for clay resources intended for use as supplementary cementitious material, Mater. Struct. 55 (2022) 149, https://doi.org/10.1617/s11527-022-01973-1.

[19] P. Ptáček, F. Šoukal, T. Opravil, M. Nosková, J. Havlica, J. Brandštetr, The kinetics of Al–Si spinel phase crystallization from calcined kaolin, J. Solid State Chem. 183 (2010) 2565–2569, https://doi.org/10.1016/j.jssc.2010.08.030.

[20] B. Sonuparlak, M. Sarikaya, I.A. Aksay, Spinel phase formation during the 980oC exothermic reaction in the kaolinite-to-mullite reaction series, J. Am. Ceram. Soc. 70 (1987) 837–842, https://doi.org/10.1111/j.1151-2916.1987.tb05637.x.

[21] G.W. Brindley, M. Nakahira, The Kaolinite-MulIite reaction series: ill, the high-temperature phases, J. Am. Ceram. Soc. 42 (1959) 319–324, https://doi.org/10.1111/j.1151-2916.1959.tb14316.x.

[22] I.M. Low, R.R. McPherson, The structure and composition of Al-Si spinel, J. Mater. Sci. Lett. 7 (1988) 1196–1198, https://doi.org/10.1007/BF00722336.

[23] Y.-F. Chen, M.-C. Wang, M.-H. Hon, Phase transformation and growth of mullite in kaolin ceramics, J. Eur. Ceram. Soc. 24 (2004) 2389–2397, https://doi.org/10.1016/S0955-2219(03)00631-9.

[24] J. Rocha, J. Klinowski, 295i and 27A1 Magic-Angle-Spinning NMR Studies of the Thermal Transformation of Kaolinite, (n.d.) vol. 8..

[25] ASTM C1897, Standard Test Methods for Measuring the Reactivity of Supplementary Cementitious Materials by Isothermal Calorimetry and Bound Water Measurements, 2020, https://doi.org/10.1520/C1897-20.2.

[26] A. Guatame-García, M. Buxton, F. Deon, C. Lievens, C. Hecker, Toward an on-line characterization of kaolin calcination process using short-wave infrared spectroscopy, Miner. Process. Extr. Metall. Rev. 39 (2018) 420–431, https://doi.org/10.1080/08827508.2018.1459617.

[27] S. Speil, L. Berkelhamer, J. Pask, B. Davies, Differential Thermal Analysis, its Applications in Clays and Other Aluminous Minerals, US department of the interior, Bureau of mines, Washington, 1945 ark:/67531/metadc66463.

[28] T. Ondro, A. Trník, Kinetic Behaviour of Thermal Transformations of Kaolinite, Smolenice, Slovakia, 2018, 020033, https://doi.org/10.1063/1.5047627.

[29] Y. Han, W. Liu, J. Zhou, J. Chen, Interactions between kaolinite Al-OH surface and sodium hexametaphosphate, Appl. Surf. Sci. 387 (2016) 759–765, https://doi.org/10.1016/j.apsusc.2016.07.002.

[30] K. Scrivener, R. Snellings, B. Lothenbach, A practical guide to microstructural analysis of cementitious materials, 2016, https://doi.org/10.7693/wl20150205, 540.

[31] A. Wong, M.E. Smith, V. Terskikh, G. Wu, Obtaining accurate chemical shifts for all magnetic nuclei (^{1} H, ^{13} C, ^{17} O, and ^{27} Al) in tris(2,4-pentanedionato- O , O') aluminium(III) — a solid-state NMR case study, Can. J. Chem. 89 (2011) 1087–1094, https://doi.org/10.1139/v11-046.

[32] A. Goldbourt, P. Madhu, Multiple-quantum magic-angle spinning: high-resolution solid state NMR spectroscopy of half-integer quadrupolar nuclei, in: Curr. Dev. Solid State NMR Spectrosc., Springer, Vienna, 2002, https://doi.org/10.1007/978-3-7091-3715-4_2, 17.54.

[33] D. Massiot, F. Fayon, M. Capron, I. King, S. Le Calvé, B. Alonso, J.-O. Durand, B. Bujoli, Z. Gan, G. Hoatson, Modelling one- and two-dimensional solid-state NMR spectra, Magn. Reson. Chem. 40 (2002) 70–76, https://doi.org/10.1002/mrc.984.

[34] M.S. Prasad, K.J. Reid, H.H. Murray, Kaolin: processing, properties and applications, Appl. Clay Sci. 6 (1991) 87–119, https://doi.org/10.1016/0169-1317(91)90001-.

[35] F. Zunino, K. Scrivener, Increasing the kaolinite content of raw clays using particle classification techniques for use as supplementary cementitious materials, Construct. Build. Mater. 244 (2020), 118335, https://doi.org/10.1016/j.conbuildmat.2020.118335.

[36] A. Plançon, R.F. Giese, R. Snyder, The Hinckley index for kaolinites, Clay Miner. 23 (1988) 249–260, https://doi.org/10.1180/claymin.1988.023.3.02.

[37] P. Aparicio, E. Galán, R.E. Ferrell, A new kaolinite order index based on XRD profile fitting, Clay Miner. 41 (2006) 811–817, https://doi.org/10.1180/0009855064140220.

[38] I.M.R. Bernal, M.A.G. Aranda, I. Santacruz, A.G. De La Torre, A. Cuesta, Early-age reactivity of calcined kaolinitic clays in LC ^{3} cements: a multitechnique investigation including pair distribution function analysis, J. Sustain. Cem.-Based Mater. 12 (2023) 721–735, https://doi.org/10.1080/21650373.2022.2117248.

[39] F. Zunino, E. Boehm-Courjault, K. Scrivener, The impact of calcite impurities in clays containing kaolinite on their reactivity in cement after calcination, Mater. Struct. 53 (2020) 44, https://doi.org/10.1617/s11527-020-01478-9.

[40] J.-P. Gilson, G.C. Edwards, A.W. Peters, K. Rajagopalan, R.F. Wormsbecher, T. G. Roberie, M.P. Shatlock, Penta-co-ordinated aluminium in zeolites and aluminosilicates, J. Chem. Soc. Chem. Commun. 91 (1987), https://doi.org/10.1039/c39870000091.

[41] N. Garg, J. Skibsted, Dissolution kinetics of calcined kaolinite and montmorillonite in alkaline conditions: evidence for reactive Al(V) sites, J. Am. Ceram. Soc. 102 (2019) 7720–7734, https://doi.org/10.1111/jace.16663.
[42] D. Massiot, P. Dion, J.F. Alcover, F. Bergaya, 27Al and 29Si MAS NMR study of kaolinite thermal decomposition by controlled rate thermal analysis, J. Am. Ceram. Soc. 78 (1995) 2940–2944, https://doi.org/10.1111/j.1151-2916.1995.tb09067.x.
[43] F. Zunino, K. Scrivener, Oxidation of pyrite (FeS2) and troilite (FeS) impurities in kaolinitic clays after calcination, Mater. Struct. 55 (2022) 9, https://doi.org/10.1617/s11527-021-01858-9.
[44] P. Romero, N. Garg, Evolution of kaolinite morphology upon exfoliation and dissolution: evidence for nanoscale layer thinning in metakaolin, Appl. Clay Sci. 222 (2022), 106486, https://doi.org/10.1016/j.clay.2022.106486.
[45] R.E. Grim, R.A. Rowland, Differential thermal analysis of clay minerals and other hydrous materials. Part 2, Am. Mineral. 27 (1942) 801–818.